

1  
2  
3  
4  
5  
6  
7  
8  
9  
10  
11  
12  
13  
14  
15  
16  
17  
18  
19  
20  
21  
22  
23  
24  
25  
26  
27  
28  
29  
30  
31  
32

THE SECOND FRACTURE OCCURS AT THE SITE OF  
LOWEST SUB-ENTHESEAL TRABECULAR BONE  
VOLUME FRACTION ON THE TIBIAL PLATEAU.

by

*William Mullins<sup>1</sup>, Gavin E. Jarvis<sup>1</sup>, Daniel Oluboyede<sup>1</sup>, Linda Skingle<sup>4</sup>, Ken Poole<sup>4</sup>, Tom  
Turmezei<sup>2</sup>, Cecilia Brassett<sup>1</sup>.*

1. Human Anatomy Teaching Group, Department of Physiology, Development and Neuroscience,  
University of Cambridge
2. Consultant Musculoskeletal Radiologist, Norfolk and Norwich University Hospitals NHS Trust
3. Department of Medicine, Cambridge NIHR Biomedical Research Centre, University of  
Cambridge

Final draft: 24<sup>th</sup> May 2020

Contact E-mail: [wjm40@cam.ac.uk](mailto:wjm40@cam.ac.uk)

33 **Abstract**

34

35 In a series of human cadaveric experiments, Dr. Paul Segond first described the avulsion injury occurring at the  
36 anterolateral tibial plateau that later took his name. The fracture is thought to arise as a consequence of  
37 excessive tibia internal rotation which often also elicits damage to other connective tissue of the knee. The exact  
38 mechanism behind the avulsion is, however, unclear. A number of ligamentous structures have been proposed in  
39 separate studies to insert into the Segond fragment. Suggestions include the iliotibial band (ITB), biceps femoris  
40 and the controversial 'anterolateral ligament' (ALL). Despite increasing knowledge of tibial plateau bony  
41 microarchitecture in both healthy and disease states, no studies have yet, to our knowledge, considered the role  
42 of tibial sub-enthesal bone structure in pathogenesis of the Segond fracture. The goal of this study was thus to  
43 elucidate the differences in trabecular properties at regions across the tibial plateau in order to provide an  
44 explanation for the susceptibility of the anterolateral region to avulsion injury. Twenty human tibial plateaus  
45 from cadaveric donors were dissected and imaged using a Nikon-XTH225- $\mu$ CT scanner with  $<80\ \mu\text{m}$  isotropic  
46 voxel size. Scans were reconstructed using MicroView 3D Image Viewer and Analysis Tool. Subsequent virtual  
47 biopsy at ten anatomically defined regions of interest (ROI) generated estimates of bone volume fraction ('bone  
48 volume divided by total volume' (BV/TV)). The overall mean BV/TV value across all 20 tibiae and all 10 ROIs  
49 was 0.271. Univariate repeated-measurements ANOVA demonstrated that BV/TV values differed between  
50 ROIs. BV/TV values at the Segond site ( $S\alpha$ ,  $S\beta$  or  $S\gamma$ ) were lower than all other ROIs at 0.195, 0.192 and 0.193  
51 respectively. This suggests that, notwithstanding inter- and intra-specimen variation, the Segond site tends to  
52 have a lower trabecular bone volume fraction than enthesal sites elsewhere on the tibia. Since BV/TV  
53 correlates with tensile and torsional strength, the lower BV/TV at the Segond site could equate to a region of  
54 local weakness in certain individuals which predisposes them to an avulsion injury following the application of  
55 force from excessive internal rotation. The low BV/TV recorded at the Segond site also challenges the idea that  
56 the fracture occurs due to pull from a discrete 'anterolateral ligament', as the tension exerted focally would be  
57 expected to elicit a hypertrophic response in line with Frost's Mechanostat hypothesis. Our data would instead  
58 agree with the aforementioned reports of the fibrous band at the Segond site being part of a broader insertion of  
59 an 'anterolateral complex'.

60

61

62

63

64

65

66

67

68

69

70

71

72

73

74

75

76

77

78

79

80

81

82

83

84

85

86

87

88

89

90

91

## 92 Introduction

### 93 The Segond Fracture

94 In a series of human cadaveric experiments, Dr. Paul Segond (1879) first described the avulsion injury occurring  
95 at the anterolateral tibial plateau that later took his name. The Segond fracture commonly occurs alongside local  
96 soft tissue injury; studies have shown 75-100% of injuries result in anterior cruciate ligament (ACL) tear and  
97 66-70% result in meniscal damage as a consequence of the trauma (Dietz et al. 1986; Goldman et al. 1988). It  
98 has been suggested that this is due to soft tissue structures of the anterolateral region being placed under a  
99 comparable degree of strain to intracapsular ligaments by tibial internal rotation (Dodds et al. 2014). Damage to  
100 these anterolateral soft tissue structures have been shown to elicit a positive pivot shift phenomenon – a finding  
101 classically indicative of ACL tear (Bull et al. 1999; Hughston et al. 1976) – suggesting this tissue is involved in  
102 maintaining similar axes of knee stability as the ACL. Moreover, anterolateral structures have been suggest to  
103 have a more important role in resisting internal rotation because of the larger moment arm they carry compared  
104 to the more centrally-located ACL (Amis, 2017).

105  
106  
107  
108 Almost a century after Segond's original reports of a "*pearly, resistant, articular fibrous band*" (Segond 1879,  
109 p14) that was placed under strain by the same internal rotation forces that are resisted by the ACL, Kaplan  
110 (1958) proposed that deep fibres of the iliotibial band (ITB) insert into the Segond fragment. Later groups  
111 suggested other insertions, including part of the short head of biceps femoris (Terry and LaPrade, 1996) and an  
112 extension of the lateral capsular ligament (Johnson, 1979; Woods et al. 1979). These observations underlie the  
113 classification of the injury as an avulsion, insofar as the mechanism involves a soft tissue structure pulling on  
114 the bone at the site of insertion. More detailed analysis later suggested that the fibres which insert into the  
115 Segond fragment may be considered - functionally or anatomically – part of a distinct ligamentous structure: the  
116 'anterolateral ligament' (ALL). Comparison of radiological data from patients with a possible Segond fracture  
117 with cadaveric reports of the ALL's tibial insertion demonstrated that the avulsion occurred at the exact site of  
118 ALL insertion (Claes et al. 2014). Biomechanical analysis has shown that, like the ACL, the ALL is an  
119 important stabiliser of internal rotation, and may play a more important role in stability during knee flexion  
120 (Parsons et al. 2015).

121  
122 There is a lack of consensus surrounding the incidence of the ALL in adult knees, with some authors arguing for  
123 inexistence whilst others claiming a presence in 100% of knees (Ariel de Lima et al. 2019). Arguments against  
124 include MRI data has suggested that the ALL is inseparable from neighboring lateral collateral ligament (LCL)  
125 and ITB (Porrino et al. 2015). It follows that the Segond fragment could, therefore, receive insertion from one of  
126 several closely-opposed ligamentous and capsular attachments within the 'anterolateral complex' (Shaikh et al.  
127 2017). Knowledge of the anatomy of this region is important for characterising the mechanisms of traumatic  
128 internal structural derangement and to help guide anterolateral capsule repair – an intervention which has been  
129 shown to restore rotational stability and correct pivot shift (Ferretti et al. 2017b).

### 130 MicroCT and Virtual Biopsy

131  
132  
133 Micro-computed tomography ( $\mu$ CT) is an imaging modality which is limited to scans of smaller scale specimens  
134 than a typical clinical CT scanner. It is, however, able to do so at a much higher resolution with a pixel size in  
135 the order of 10s compared to 100s of microns. The detail of the acquired image allows for repeated 'virtual  
136 biopsy' of a specimen in a non-destructive manner, while the richness of information also allows sampling of  
137 the image data volume at locations that can be selected from multiple orthogonal viewing planes.  $\mu$ CT has  
138 advantages over dual-energy X-ray absorptiometry (DXA) for assessment of bone mineral density (BMD) due  
139 to its ability to incorporate three dimensions in the reconstructed imaging in addition to the superior resolution.  
140 It is therefore used as a means of conferring validity to novel DXA techniques attempting to mimic the  
141 resolution of other imaging modalities (Briggs et al. 2010). DXA remains the clinical modality of choice for  
142 assessment of BMD because of the lower radiation dose, relatively low cost and ability to scan larger specimens  
143 (Kleerekoper and Nelson, 1997).  $\mu$ CT is instead currently restricted - in human imaging research - to analysis of  
144 ex vivo specimens.

145  
146 Variations in apparent bone trabecular volume fraction are related by a power-law function to bone tensile and  
147 torsional strength (Kaplan et al. 1985; Sarin et al. 1999). Trabecular bone has been shown to have a significantly  
148 lower tensile strength compared to compression strength, explaining why the force of injury in avulsion  
149 fractures is typically much lower than that seen in other types of fracture (Kaplan et al. 1985). As a precedent,  
150  $\mu$ CT has been used to quantify the correlation between trabecular bone volume fraction and strength parameters  
151 - namely, Young's modulus, yield stress and ultimate stress - in cadaveric tibiae (Lancianese et al. 2008).

152 Trabecular bone volume fraction (bone volume over total volume, BV/TV, expressed in %) recorded using  $\mu$ CT  
153 has also been used as a means of predicting strength and stiffness in both normal and pathological trabecular  
154 bone (Nazarian et al. 2008).

155

### 156 Gaps in the Field and Aims of the Current Study

157

158 Despite increasing knowledge of tibial plateau bony microarchitecture in both healthy and disease states, no  
159 studies have yet, to our knowledge, considered the role of tibial sub-enthesal bone structure in pathogenesis of  
160 the Segond fracture. The goal of this study was thus to elucidate the differences in trabecular properties  
161 according to  $\mu$ CT analysis at regions across the tibial plateau and quantify the relative bone densities underlying  
162 each enthesis. When referencing enthesal sites, we intend to discuss each as a functional organ – including  
163 adjacent trabecular bone structure in addition to the cortex which receives the insertion. We hypothesised that  
164 BV/TV at the Segond site was lower than other entheses across the plateau, explaining the propensity for  
165 avulsion.

166

## 167 **Materials and Methods**

168

### 169 Dissection

170

171 Lower limb specimens were randomly selected for dissection from human cadavers. All donors had provided  
172 written consent before decease for their bodies to be used for anatomical research, in compliance with the  
173 Human Tissue Act 2004. Specimens with evidence of overt knee trauma, surgery or degenerative joint disease  
174 were excluded. We further eliminated specimens whose records stated the cause of death was from breast,  
175 prostate or lung cancer; as these are the most common cancers which seed bony metastases (Mundy, 2002;  
176 Svensson et al. 2017). Fifteen female (age range, 72-99; mean(SD) age, 87.2(8.4) years) and five male (age  
177 range, 82-93; mean(SD) age 87.4(5.3) years) donors passed the initial screening and were thereby included in  
178 the study. A standardised dissection procedure was used for each specimen, involving removal of skin and soft  
179 tissues, as well as disarticulation of the knee joint. The isolated tibial plateaus remained connected to the  
180 adjacent fibulae by their associated ligaments. Both were cut to around 10cm in length such that they would fit  
181 within the apparatus for loading into the  $\mu$ CT scanner. Tendons were left in place to act as reference points for  
182 later virtual biopsy.

183

### 184 MicroCT Scanning

185

186 Specimens were packed individually into a polystyrene holding container such that they would stand upright  
187 independently and remain stationary during rotation of the platform within the scanner. The holding containers  
188 were loaded into and imaged using a Nikon XTH225  $\mu$ CT scanner (Nikon Metrology UK Ltd., Derby, UK),  
189 with  $<80 \mu\text{m}$  isotropic voxel size. The scan time for each sample was approximately 25 minutes. DICOM  
190 imaging output was exported for viewing and analysis.

191

### 192 Virtual Biopsy

193

194 Scans were loaded onto the open-source MicroView 3D Image Viewer and Analysis Tool (Parallax Innovations  
195 Inc., Ilderton, Ontario, Canada). Individual slices were reconstructed into a 3D model of each tibial plateau (see  
196 Fig. 1). We chose to compare sub-enthesal trabecular properties at the Segond site with other entheses across  
197 the tibial plateau and fibular head. Spheres of 5 mm diameter were constructed to define the portion of the bone  
198 to be analysed. These 'regions of interest' (ROIs) were positioned to underlie ten enthesal or compression sites  
199 across the tibial plateau (numbered below). Precise locations below refer to the centre-point of the virtual biopsy  
200 ROI. They were chosen based on preliminary measurements of where the sub-enthesal trabecular bone  
201 appeared to have the highest volume fraction at each site.

202

- 203 1. Anterior cruciate ligament (ACL) insertion - 50% of the medial-lateral (ML) axis of the insertion  
204 (section 'D' in Fig. 1a), 25% along anterior-posterior (AP) axis from the anterior-most point of the  
205 ACL insertion.
- 206 2. Posterior cruciate ligament (PCL) insertion - 50% of the ML axis (section 'D' in Fig. 1a) at the  
207 posterior/inferior-most insertion point of the PCL.
- 208 3. Patellar tendon (PT) insertion - 50% of the ML axis of the tibial tuberosity, 77.5% the superior-inferior  
209 distance along the PT insertion (section 'C' in Fig. 1b).
- 210 4. Medial tibial condyle (MTC) - 16% of ML axis of the tibial plateau from the medial edge, 55% of AP  
211 axis (section 'A' in Fig. 1a) from anterior edge.

- 212 5. Lateral tibial condyle (LTC) - 10% of ML axis of the tibial plateau from the lateral edge, 65% of AP  
213 axis (section 'A' in Fig. 1a) from anterior edge.
- 214 6. Lateral collateral ligament (LCL) insertion - 50% of the distance across the ML width of the proximal-  
215 most insertion point of the LCL (section 'B' in Fig. 1a).
- 216 7. Segond site  $\alpha$  ( $S\alpha$ ) - 50% of the AP distance from Gerdy's tubercle to the posterior aspect of the fibular  
217 head (section 'B' in Fig. 1a), 7.8 mm from the tibial plateau in the proximal-distal plane. Vertical depth  
218 from plateau chosen based on previous literature which showed the mean distance of the midpoint of  
219 the fracture to the tibial plateau to be  $7.8 \pm 2.7$  mm (Shaikh et al. 2017).
- 220 8. Segond site  $\beta$  ( $S\beta$ ) - 2.5 mm anterior to  $S\alpha$ .
- 221 9. Segond site  $\gamma$  ( $S\gamma$ ) - 2.5 mm posterior to  $S\alpha$ .
- 222 10. Iliotibial band (ITB) insertion - same vertical depth as (7), centered 50% of the ML width of Gerdy's  
223 tubercle.

224  
225 The relative locations of the ROIs detailed above are shown in Fig. 2. The medial collateral ligament could not  
226 be included as its insertion varied between tibiae and thus could not be reliably found using the methodology  
227 above. The medial and lateral condyles represent compression zones: included as data to add insight into the  
228 relationship between compression force and bone volume. The Segond fracture has been stated as having an  
229 average length of 10 mm (Shaikh et al. 2017). Due to the 5 mm diameter sphere which defined the portion being  
230 measured, 3 ROIs were used to sample the full diameter of the Segond site and to map any variations that might  
231 be across this region:  $S\alpha$ ,  $S\beta$  and  $S\gamma$ .

232  
233 Using MicroView software, BV/TV was measured at each ROI. The value represented the fraction of the ROI  
234 occupied by trabecular bone. A value of 0 would represent thin air, and a value towards 1 would be found in  
235 near-solid cortical bone. At each ROI, a total of five replicate measurements were taken by moving the  
236 measuring tool 1mm from the calculated centre-point in four opposing directions on the cortical axis – for  
237 example, at the ACL site, the repeat measurements were taken 1mm anterior, posterior, medial and lateral from  
238 the calculated centre point. Crucially, cortical bone was avoided during repeat measurements by keeping depth  
239 in relation to the cortex constant for each repeat measurement. This was necessary so that the higher BV/TV of  
240 cortical bone did not inflate the measurement of bone volume fraction of the underlying trabecular bone.

#### 241 Statistical analysis

242  
243 Five replicate BV/TV measurements were obtained using MicroView for each ROI in each specimen. The  
244 means of the replicates represent 10 ROI values (mean BV/TV) for each specimen. Descriptive statistics and  
245 analyses were performed on these values as described.

246  
247 Univariate repeated-measurements ANOVA (ROI = within-subject variable) using the Greenhouse-Geisser  
248 correction for sphericity was performed using IBM® SPSS Statistics v.25 and Microsoft Excel to evaluate  
249 differences between ROIs. Normality of residuals was evaluated using the D'Agostino Pearson test (GraphPad  
250 Prism 8.4.2). Statistical results presented are from log-transformed data for all 10 ROIs ( $n = 200$ ) and a  
251 condensed dataset ( $n = 160$ ) in which  $S\alpha$ ,  $S\beta$  or  $S\gamma$  were replaced with a single value (SEG) equalling the mean  
252 of the three separate values. Pairwise within-subject contrasts between ROIs and either  $S\alpha$  or SEG values were  
253 performed with a Bonferroni adjustment.

#### 254 **Results**

255  
256 Mean BV/TV values for each ROI are shown in Table 1. In 15 of the 20 tibiae, the lowest intra-specimen mean  
257 BV/TV was found at the Segond site (range = 0.092-0.262, recorded at either  $S\alpha$ ,  $S\beta$  or  $S\gamma$ ). In the remaining 5  
258 tibiae, the lowest intra-specimen mean BV/TV value was found at either the LCL (0.128 and 0.171), ITB  
259 (0.196) or ACL (0.171 and 0.259). The highest BV/TV was found in 12 tibiae at the PT (range = 0.299-0.655), 6  
260 at the MTC (range = 0.369-0.595) and 2 at the LTC (0.366 and 0.400). In addition to these intra-specimen  
261 differences, tibiae also varied in their mean specimen BV/TV (range = 0.185-0.363; mean = 0.271).

262  
263 Pooled mean BV/TV values (mean of ROI values from all 20 tibiae) at the Segond site ( $S\alpha$ ,  $S\beta$  or  $S\gamma$ ) was the  
264 lowest of all the ROIs at 0.195, 0.192 and 0.193 respectively. This suggests that despite the inter- and intra-  
265 specimen variation in mean BV/TV, the Segond site tends to have a lower trabecular bone volume fraction than  
266 enthesal sites elsewhere on the tibia.

267  
268 Mean BV/TV and pooled mean BV/TV data are displayed graphically in Fig. 3a and logged mean BV/TV data  
269 in Fig. 3b. Distribution of residuals ( $n = 200$ ) from repeated-measures ANOVA of non-logged data deviated  
270  
271

272 from normality (D'Agostino-Pearson test,  $K2 = 23.37$ ,  $P < 0.0001$ ) and so analysis was performed on logged  
273 data ( $K2 = 6.67$ ,  $P = 0.0356$ ). This revealed a clear difference between ROIs ( $F_{5,4,102.2} = 64.97$ ,  $P < 0.0001$ ).  
274 Within-subject contrasts to  $S\alpha$  yielded the following  $P$  values (Bonferroni-adjusted):  $S\beta > 0.99$ ;  $S\gamma > 0.99$ ; ACL  
275 = 0.0031; LCL = 0.029; ITB, PCL, LTC, MTC & PT  $< 0.0001$ .

276  
277  $S\alpha$ ,  $S\beta$  and  $S\gamma$  ROIs were sampled from loci in very close proximity. Not surprisingly, there was a strong  
278 correlation between these values ( $\rho_{(S\alpha \vee S\beta)} = 0.93$ ,  $\rho_{(S\alpha \vee S\gamma)} = 0.89$ ;  $\rho_{(S\beta \vee S\gamma)} = 0.86$ ). Since this may have influenced  
279 residual distribution, a mean value for the Segond region (SEG) was calculated from  $S\alpha$ ,  $S\beta$  and  $S\gamma$  values, and  
280 substituted the three discrete values in a parallel analysis. The distribution of residuals from the analysis of logged  
281 values ( $n = 160$ ) conformed well to normality ( $K2 = 2.49$ ,  $P = 0.29$ ) whereas the non-logged data retained an  
282 apparent deviation ( $K2 = 12.93$ ,  $P = 0.0016$ ).

283  
284 Repeated-measures ANOVA of logged data with the substituted SEG values (condensed dataset) also revealed a  
285 convincing difference between ROIs ( $F_{4,8,91.2} = 53.10$ ,  $P < 0.0001$ ). Within-subject contrasts to SEG yielded the  
286 following  $P$  values (Bonferroni-adjusted): ACL = 0.0015; LCL = 0.013; ITB, PCL, LTC, MTC & PT  $< 0.0001$ .  
287 Fig. S1a & b show the condensed SEG-substituted data.

288  
289 A higher incidence of Segond fractures has been reported both in men (Claes et al. 2014) and in right-sided tibiae  
290 (Ferretti et al. 2017a). Our study was not designed to evaluate any effect of sex or side, but used an opportunity  
291 sample from cadavers available for anatomical dissection. Nevertheless, among the specimens, 13 were left-sided  
292 (10 female, 3 male) and 7 right-sided (5 female, 2 male). Secondary analyses to explore the effect of SEX or SIDE  
293 were performed using the repeated-measures ANOVA (with Type II sum of squares) described above with  
294 incorporation of either SEX or SIDE as a between-subjects factor. Interpretation of the results must account for  
295 the opportunistic nature of the sample; nevertheless our data provide no support for the existence of a difference  
296 in trabecular bone density between sexes ( $F_{1,18} = 2.24$ ,  $P = 0.152$ ) or sides ( $F_{1,18} = 0.345$ ,  $P = 0.564$ ). Neither was  
297 there evidence of an interaction between ROIs and either SEX ( $F_{5,4,96.7} = 0.64$ ,  $P = 0.68$ ) or SIDE ( $F_{5,3,96.1} = 0.32$ ,  
298  $P = 0.91$ ). (Analyses were performed on logged values of the full data set. No differences were observed when  
299 performed on the condensed data set.) Furthermore, there was no evidence that sex or side contributed to  
300 deviations from normality of the non-grouped data (residual distribution ( $n = 200$ ) including SEX:  $K2=8.92$ ,  $P =$   
301  $0.0116$ ; and including SIDE:  $K2 = 6.32$ ,  $P = 0.0423$ ).

## 303 Discussion

304  
305 This study shows that BV/TV at the Segond site is significantly lower than other entheses across the tibial  
306 plateau. As mentioned previously, BV/TV has been shown to correlate with tensile and torsional strength – the  
307 forces putatively responsible for avulsion fractures (Kaplan et al. 1985; Sarin et al. 1999). The lower BV/TV at  
308 the Segond site could, therefore, equate to a region of local weakness in certain individuals which predisposes  
309 them to the avulsion injury following excessive internal rotation of the knee. This ‘weakest link’ hypothesis  
310 agrees with findings that the minimum BV/TV value for a specimen gave a far higher predictive power than the  
311 average specimen BV/TV in predicting the probability of mechanical failure of trabecular bone (Nazarian et al.  
312 2006). Given the complex ligamentous and capsular arrangements around the knee joint, it is reasonable to  
313 assume that several structures would be placed under strain during internal rotation. The avulsion could,  
314 therefore, arise from the trabecular bone at the Segond site being a highly susceptible locus on the tibial plateau,  
315 with other injuries accumulating sequentially following progressive increases in internal rotational force. Since  
316 avulsions elsewhere on the tibial plateau occur at a much lower incidence (Bali et al. 2012; Caggiari et al. 2020;  
317 Edmonds et al. 2015), it may be the case that a higher enthesal BV/TV means the weakest link lies in the  
318 substance of the ligament, causing a mid-substance tear to be more likely than an avulsion fracture.

319  
320 Segond's original work described an extreme tractional force along a “*fibrous band*” on the anterolateral aspect  
321 of the knee during tibial internal rotation (Segond 1879, p14). The low BV/TV we recorded at the Segond site  
322 challenges the hypothesis that this band represents a discrete ligament, such as the ALL, as the tension exerted  
323 focally by a single ligament would be expected to elicit a hypertrophic response in line with Frost's  
324 Mechanostat hypothesis (Frost, 2000). The Mechanostat argues that trabecular networks show a homeostatic  
325 response to load, including force from both compression and tension. This would explain why our highest  
326 recorded BV/TV values were found at the MTC/LTC and PT – ROIs subject to the greatest compressive and  
327 tensile forces respectively. The Mechanostat hypothesis would argue that a locally low BV/TV would be found  
328 in a region subject to a low force per unit area. Our data would, therefore, agree with the aforementioned reports  
329 of Segond's fibrous band being part of a broader, less discrete insertion - including fibres from the ITB and  
330 lateral joint capsule (Shaikh et al. 2017) – which has the effect of distributing the force from internal rotation  
331 over a larger area.

332  
333 The limitations of this study include: (1) Our donor population were all over the age of 70 years, meaning the  
334 average BV/TV was unlikely to reflect population means across all ages. A solution here would be to source  
335 younger donors or perhaps tibiae from amputee donors to infer whether the trend in BV/TV continues across all  
336 age ranges. (2) The osteoporosis status of the donors was not included in their records and thus we were unable  
337 to categorise subjects by those with pathological demineralisation of bone. We also cannot be certain that  
338 individuals in the study did not have any previous trauma to their knee that might have resulted in ligamentous,  
339 capsular, or bony injury that might affect these results. (3) Virtual biopsy at the Segond site relied on theoretical  
340 constructs alone, based on parameters cited in previous literature. As a result, anatomical variation of the  
341 individual specimens may have resulted in biopsies being taken from locations which were not truly represent  
342 the fracture site. Our results would be ideally validated using a longitudinal study to observe which donor  
343 subgroups are at risk of avulsion injury. This would, however, not be possible using the current methodology  
344 since  $\mu$ CT is limited to imaging smaller, ex-vivo specimens. A first step would be to mirror the data in human  
345 subjects using a technique such as DXA imaging, however, at present, the resolution of these alternate imaging  
346 methods falls short of  $\mu$ CT.

#### 347 **Abbreviations**

348  
349  
350 ACL: Anterior cruciate ligament  
351 ALL: Anterolateral ligament  
352 AP: Anterior-posterior  
353 BV/TV: Bone volume divided by total volume  
354 DICOM: Digital Imaging and Communications in Medicine  
355 DXA: Dual-energy X-ray absorptiometry  
356 ITB: Iliotibial band  
357 LCL: Lateral collateral ligament  
358 LTC: Lateral tibial condyle  
359 ML: Medial-lateral  
360 MTC: Medial tibial condyle  
361 PCL: Posterior cruciate ligament  
362 PT: Patella tendon  
363 ROI: Region of interest  
364  $S\alpha$ : Segond site  $\alpha$   
365  $S\beta$ : Segond site  $\beta$   
366  $S\gamma$ : Segond site  $\gamma$   
367 SEG: mean value from  $S\alpha$ ,  $S\beta$ , &  $S\gamma$  ROIs  
368  $\mu$ CT: Micro-computed tomography  
369

#### 370 **Acknowledgments**

371  
372 With grateful thanks to: the Anatomical Society for granting the scholarship which was used in the pilot project  
373 involving five specimens; the donors whose generosity made this research possible; Mr Jai Chitnavis,  
374 Consultant Orthopaedic surgeon, The Cambridge Knee Clinic; the staff in the Human Dissection Room,  
375 University of Cambridge (Mrs Maria Wright, Mr Darren Broadhurst and Mrs Lisa Childs); and Dr Keturah  
376 Smithson, Cambridge Biotomography Centre, Department of Zoology, University of Cambridge. Authors have  
377 no conflicts of interest to declare.  
378

#### 379 **Data Availability Statement**

380  
381 The data that support the findings of this study are available on request from the corresponding author. The data  
382 are not publicly available due to privacy or ethical restrictions.  
383

#### 384 **Author Contributions**

385  
386 Will Mullins - concept/design, acquisition of data, data analysis/interpretation, drafting of the manuscript,  
387 critical revision of the manuscript.  
388 Daniel Oluboyede - concept/design, acquisition of data, data analysis/interpretation.  
389 Gavin Jarvis - data analysis/interpretation, critical revision of the manuscript.  
390 Linda Skingle - concept/design, critical revision of the manuscript.  
391 Ken Poole - concept/design, critical revision of the manuscript.

392 Tom Turmezei - concept/design, data analysis/interpretation, critical revision of the manuscript, approval of the  
393 article.

394 Cecilia Brassett - concept/design, acquisition of data, data analysis/interpretation, critical revision of the  
395 manuscript, approval of the article.

396

## 397 References

398

399 Amis AA (2017) Anterolateral knee biomechanics. *Knee Surg Sports Traumatol Arthrosc* 25, 1015–1023.  
400 <https://doi.org/10.1007/s00167-017-4494-x>

401 Ariel de Lima D, Helito CP, Lacerda de Lima L, et al. (2019) Anatomy of the Anterolateral Ligament of the  
402 Knee: A Systematic Review. *Arthroscopy* 35, 670–681. <https://doi.org/10.1016/j.arthro.2018.09.006>

403 Bali K, Prabhakar S, Saini U, Dhillon MS (2012) Open reduction and internal fixation of isolated PCL fossa  
404 avulsion fractures. *Knee Surg Sports Traumatol Arthrosc* 20, 315–321. [https://doi.org/10.1007/s00167-](https://doi.org/10.1007/s00167-011-1618-6)  
405 [011-1618-6](https://doi.org/10.1007/s00167-011-1618-6)

406 Briggs AM, Perilli E, Parkinson IH, et al. (2010) Novel assessment of subregional bone mineral density using  
407 DXA and pQCT and subregional microarchitecture using micro-CT in whole human vertebrae:  
408 applications, methods, and correspondence between technologies. *J Clin Densitom* 13, 161–174.  
409 <https://doi.org/10.1016/j.jocd.2010.01.120>

410 Bull AM, Andersen HN, Basso O, et al. (1999) Incidence and mechanism of the pivot shift. An in vitro study.  
411 *Clin. Orthop. Relat. Res.* 219–231.

412 Caggiari G, Ciurlia E, Ortu S, et al. (2020) Osteochondral avulsion fracture of the posteromedial tibial plateau.  
413 *Trauma Case Rep* 25, 100281. <https://doi.org/10.1016/j.tcr.2020.100281>

414 Claes S, Luyckx T, Vereecke E, et al. (2014) The Segond fracture: a bony injury of the anterolateral ligament of  
415 the knee. *Arthroscopy* 30, 1475–1482. <https://doi.org/10.1016/j.arthro.2014.05.039>

416 Dietz GW, Wilcox DM, Montgomery JB (1986) Segond tibial condyle fracture: lateral capsular ligament  
417 avulsion. *Radiology* 159, 467–469. <https://doi.org/10.1148/radiology.159.2.3961179>

418 Dodds AL, Halewood C, Gupte CM, Williams A, Amis AA (2014) The anterolateral ligament: Anatomy, length  
419 changes and association with the Segond fracture. *Bone Joint J* 96-B, 325–331.  
420 <https://doi.org/10.1302/0301-620X.96B3.33033>

421 Edmonds EW, Fornari ED, Dashe J, et al. (2015) Results of Displaced Pediatric Tibial Spine Fractures: A  
422 Comparison Between Open, Arthroscopic, and Closed Management. *J Pediatr Orthop* 35, 651–656.  
423 <https://doi.org/10.1097/BPO.0000000000000356>

424 Ferretti A, Monaco E, Fabbri M, Maestri B, De Carli A (2017a) Prevalence and Classification of Injuries of  
425 Anterolateral Complex in Acute Anterior Cruciate Ligament Tears. *Arthroscopy* 33, 147–154.  
426 <https://doi.org/10.1016/j.arthro.2016.05.010>

427 Ferretti A, Monaco E, Wolf MR, et al. (2017b) Surgical Treatment of Segond Fractures in Acute Anterior  
428 Cruciate Ligament Reconstruction. *Orthop J Sports Med* 5, 2325967117729997.  
429 <https://doi.org/10.1177/2325967117729997>

430 Frost HM (2000) The Utah paradigm of skeletal physiology: an overview of its insights for bone, cartilage and  
431 collagenous tissue organs. *J. Bone Miner. Metab.* 18, 305–316. <https://doi.org/10.1007/s007740070001>

432 Goldman AB, Pavlov H, Rubenstein D (1988) The Segond fracture of the proximal tibia: a small avulsion that  
433 reflects major ligamentous damage. *AJR Am J Roentgenol* 151, 1163–1167.  
434 <https://doi.org/10.2214/ajr.151.6.1163>

435 Hughston JC, Andrews JR, Cross MJ, Moschi A (1976) Classification of knee ligament instabilities. Part II. The  
436 lateral compartment. *J Bone Joint Surg Am* 58, 173–179.

437 Johnson LL (1979) Lateral capsular ligament complex: anatomical and surgical considerations. *Am J Sports*  
438 *Med* 7, 156–160. <https://doi.org/10.1177/036354657900700302>

439 Kaplan EB (1958) The iliotibial tract; clinical and morphological significance. *J Bone Joint Surg Am* 40-A,  
440 817–832.

441 Kaplan SJ, Hayes WC, Stone JL, Beaupré GS (1985) Tensile strength of bovine trabecular bone. *J Biomech* 18,  
442 723–727. [https://doi.org/10.1016/0021-9290\(85\)90027-2](https://doi.org/10.1016/0021-9290(85)90027-2)

443 Kleerekoper M, Nelson DA (1997) Which bone density measurement? *J. Bone Miner. Res.* 12, 712–714.  
444 <https://doi.org/10.1359/jbmr.1997.12.5.712>

445 Lancianese SL, Kwok E, Beck CA, Lerner AL (2008) Predicting regional variations in trabecular bone  
446 mechanical properties within the human proximal tibia using MR imaging. *Bone* 43, 1039–1046.  
447 <https://doi.org/10.1016/j.bone.2008.07.247>

448 Mundy GR (2002) Metastasis to bone: causes, consequences and therapeutic opportunities. *Nat. Rev. Cancer* 2,  
449 584–593. <https://doi.org/10.1038/nrc867>



- 450 Nazarian A, Stauber M, Zurakowski D, Snyder BD, Müller R (2006) The interaction of microstructure and  
451 volume fraction in predicting failure in cancellous bone. *Bone* 39, 1196–1202.  
452 <https://doi.org/10.1016/j.bone.2006.06.013>
- 453 Nazarian A, von Stechow D, Zurakowski D, Müller R, Snyder BD (2008) Bone volume fraction explains the  
454 variation in strength and stiffness of cancellous bone affected by metastatic cancer and osteoporosis.  
455 *Calcif. Tissue Int.* 83, 368–379. <https://doi.org/10.1007/s00223-008-9174-x>
- 456 Parsons EM, Gee AO, Spiekerman C, Cavanagh PR (2015) The biomechanical function of the anterolateral  
457 ligament of the knee. *Am J Sports Med* 43, 669–674. <https://doi.org/10.1177/0363546514562751>
- 458 Porrino J, Maloney E, Richardson M, et al. (2015) The anterolateral ligament of the knee: MRI appearance,  
459 association with the Segond fracture, and historical perspective. *AJR Am J Roentgenol* 204, 367–373.  
460 <https://doi.org/10.2214/AJR.14.12693>
- 461 Sarin VK, Lobo Polefka EG, Beaupré GS, et al. (1999) DXA-derived section modulus and bone mineral  
462 content predict long-bone torsional strength. *Acta Orthop Scand* 70, 71–76.  
463 <https://doi.org/10.3109/17453679909000962>
- 464 Segond P (1879) *Recherches cliniques et expérimentales sur les épanchements sanguins du genou par entorse.*  
465 Paris: Aux bureaux du Progrès médical.
- 466 Shaikh H, Herbst E, Rahnama-Azar AA, et al. (2017) The Segond Fracture Is an Avulsion of the Anterolateral  
467 Complex. *Am J Sports Med* 45, 2247–2252. <https://doi.org/10.1177/0363546517704845>
- 468 Svensson E, Christiansen CF, Ulrichsen SP, Rørth MR, Sørensen HT (2017) Survival after bone metastasis by  
469 primary cancer type: a Danish population-based cohort study. *BMJ Open* 7, e016022.  
470 <https://doi.org/10.1136/bmjopen-2017-016022>
- 471 Terry GC, LaPrade RF (1996) The biceps femoris muscle complex at the knee. Its anatomy and injury patterns  
472 associated with acute anterolateral-antromedial rotatory instability. *Am J Sports Med* 24, 2–8.  
473 <https://doi.org/10.1177/036354659602400102>
- 474 Woods GW, Stanley RF, Tullos HS (1979) Lateral capsular sign: x-ray clue to a significant knee instability. *Am*  
475 *J Sports Med* 7, 27–33. <https://doi.org/10.1177/036354657900700107>

#### 476 **Supplementary material**

477  
478  
479 Figure S1  
480  
481  
482  
483  
484  
485  
486  
487  
488  
489  
490  
491  
492  
493  
494  
495  
496  
497  
498  
499  
500  
501  
502  
503  
504  
505  
506  
507  
508  
509

510  
511  
512

**Tables**  
**Table 1: Mean BV/TV values at each ROI in 20 tibiae**

Tibia	SEX	SIDE	S <sub>α</sub>	S <sub>β</sub>	S <sub>γ</sub>	ACL	LCL	ITB	PCL	LTC	MTC	PT	mean specimen BV/TV	SEG*
A	F	R	0.179	0.161	0.212	0.186	0.189	0.205	0.238	0.307	0.315	0.338	0.233	0.184
B	F	R	0.166	0.166	0.172	0.227	0.209	0.267	0.254	0.283	0.426	0.494	0.266	0.168
C	F	L	0.207	0.210	0.209	0.245	0.316	0.286	0.269	0.366	0.303	0.309	0.272	0.209
D	F	L	0.126	0.126	0.140	0.165	0.143	0.176	0.158	0.246	0.274	0.299	0.185	0.131
E	F	L	0.182	0.195	0.206	0.247	0.171	0.239	0.254	0.447	0.542	0.273	0.276	0.194
F	F	L	0.199	0.191	0.177	0.263	0.128	0.234	0.298	0.294	0.299	0.393	0.248	0.189
G	F	L	0.241	0.208	0.242	0.247	0.236	0.196	0.340	0.241	0.534	0.393	0.288	0.230
H	F	L	0.116	0.121	0.092	0.214	0.182	0.183	0.246	0.223	0.380	0.426	0.218	0.110
I	F	R	0.179	0.160	0.167	0.214	0.214	0.237	0.295	0.400	0.386	0.376	0.263	0.168
J	F	L	0.203	0.190	0.201	0.194	0.310	0.214	0.354	0.360	0.588	0.422	0.303	0.198
K	F	R	0.264	0.262	0.277	0.287	0.334	0.341	0.384	0.286	0.367	0.461	0.326	0.268
L	F	L	0.165	0.169	0.169	0.226	0.181	0.246	0.285	0.253	0.355	0.427	0.247	0.167
M	F	L	0.185	0.172	0.178	0.171	0.188	0.208	0.220	0.234	0.369	0.339	0.226	0.178
N	F	R	0.211	0.172	0.168	0.213	0.226	0.298	0.246	0.281	0.364	0.433	0.261	0.183
O	F	L	0.212	0.226	0.228	0.269	0.307	0.374	0.317	0.294	0.431	0.655	0.331	0.222
P	M	L	0.215	0.238	0.201	0.216	0.315	0.422	0.235	0.276	0.415	0.479	0.301	0.218
Q	M	R	0.158	0.157	0.171	0.204	0.212	0.213	0.230	0.238	0.327	0.384	0.229	0.162
R	M	L	0.222	0.219	0.193	0.312	0.272	0.211	0.305	0.430	0.424	0.460	0.305	0.211
S	M	R	0.284	0.309	0.259	0.259	0.275	0.390	0.362	0.392	0.595	0.505	0.363	0.284
T	M	L	0.184	0.194	0.190	0.229	0.237	0.334	0.270	0.262	0.483	0.430	0.281	0.189
<b>Pooled mean BV/TV</b>			0.195	0.192	0.193	0.229	0.232	0.264	0.278	0.306	0.409	0.415	0.271	0.193
<b>SD of mean BV/TV values</b>			0.041	0.045	0.041	0.038	0.062	0.073	0.055	0.069	0.096	0.086	0.043	0.041

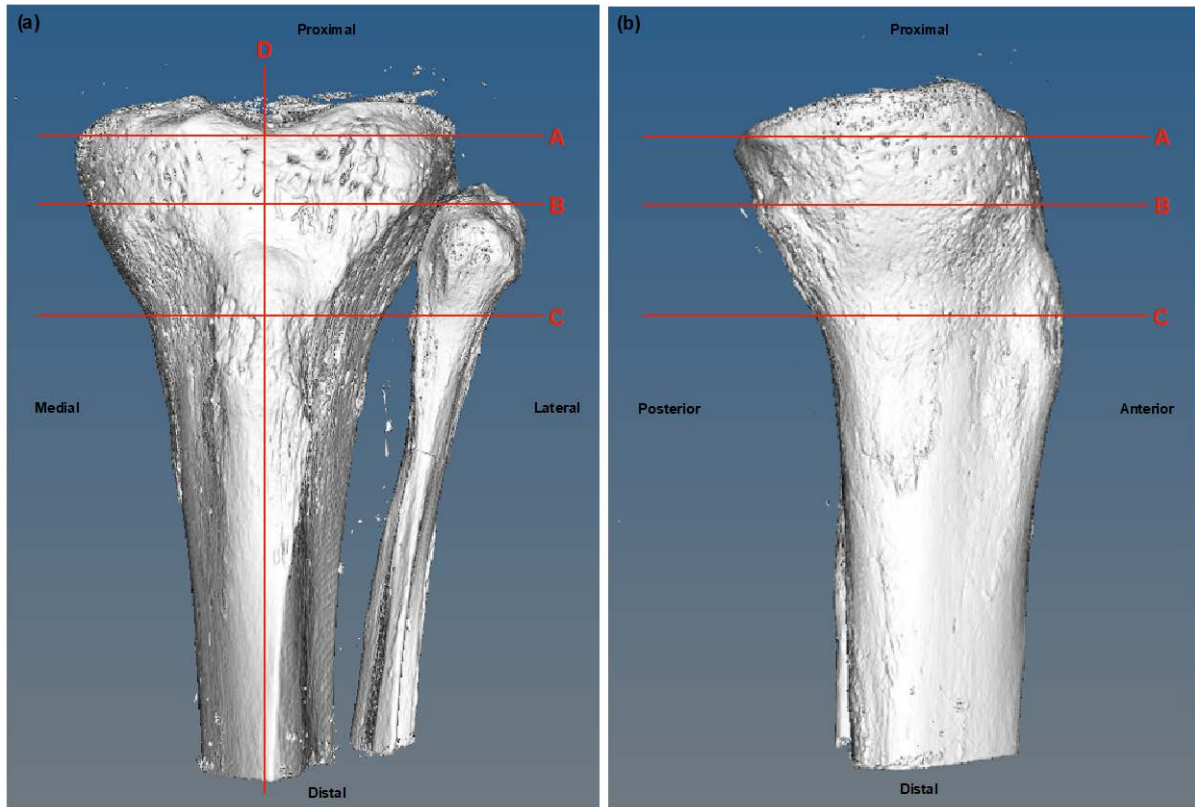
\*  $SEG = \frac{\sum(S\alpha;S\beta;S\gamma)}{3}$

513  
514  
515  
516  
517  
518  
519  
520  
521  
522  
523  
524  
525  
526  
527  
528  
529  
530  
531  
532  
533  
534  
535  
536  
537  
538  
539  
540  
541  
542  
543  
544  
545  
546  
547  
548  
549

550 **Figures**

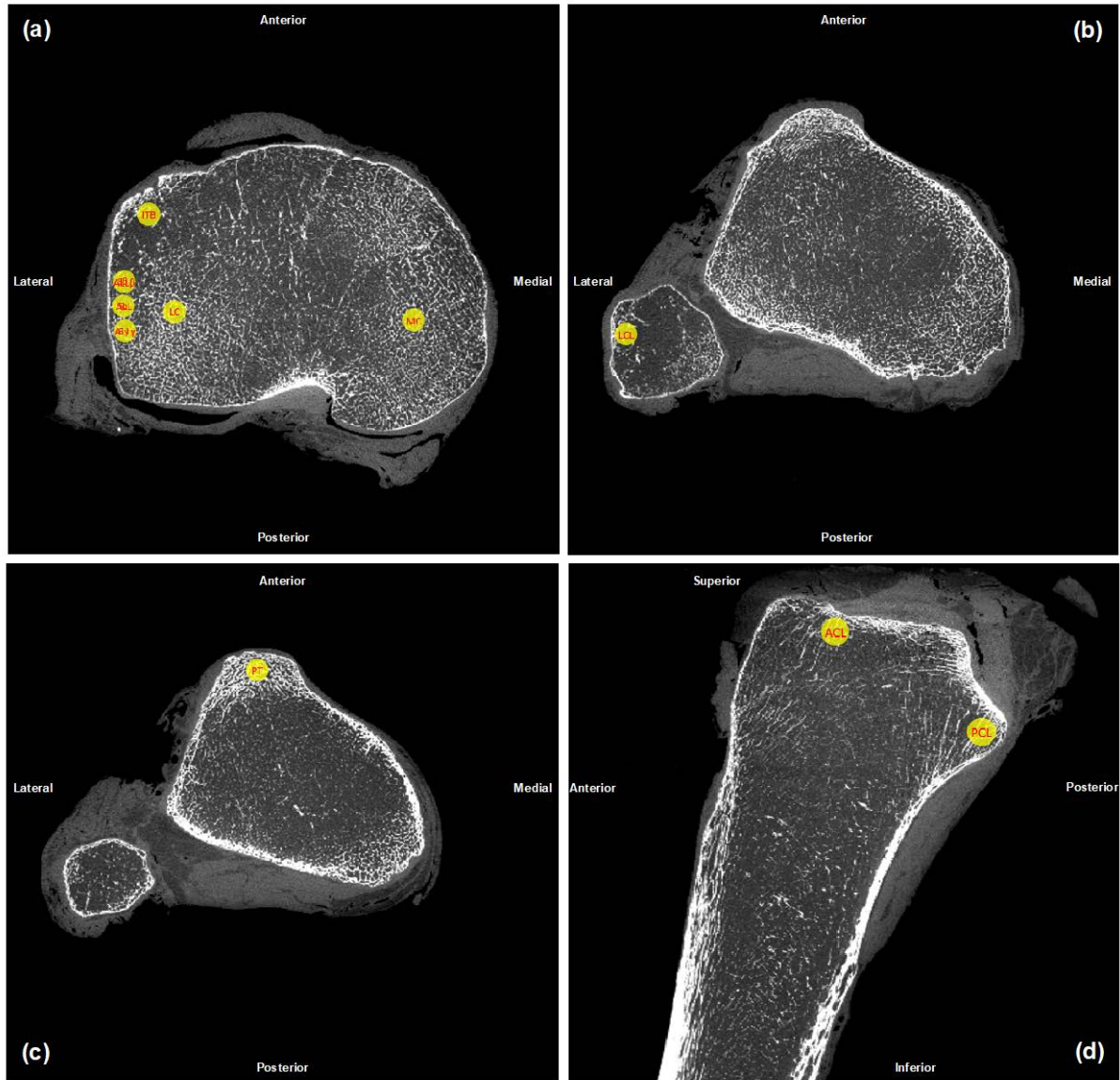
551

552 **Figure 1: Appearance of the virtual tibial plateau following reconstruction of DICOM output using**  
 553 **MicroView.** (a) Antero-posterior (AP) view of the left tibial plateau from specimen 5 (female, Age 76 years,  
 554 cause of death: heart failure). (b) Medio-lateral (ML) view of the same specimen. Letters indicate sections at  
 555 which ROIs were measured and positioned (see Fig. 2). Image taken during reconstruction on 08/03/19.



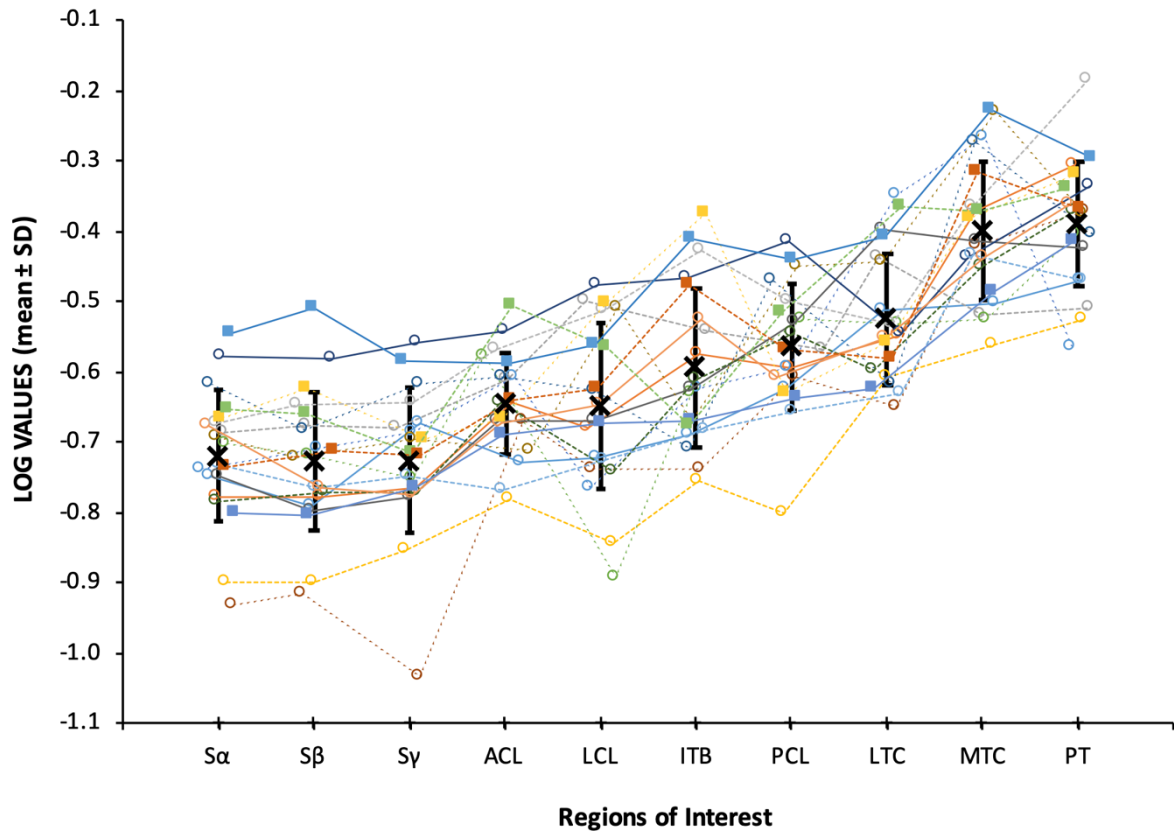
556  
 557  
 558  
 559  
 560  
 561  
 562  
 563  
 564  
 565  
 566  
 567  
 568  
 569  
 570  
 571  
 572  
 573  
 574  
 575  
 576  
 577  
 578  
 579  
 580  
 581  
 582

583 **Figure 2:  $\mu$ CT sections of a reconstructed tibial plateau showing the location of each ROI.** (a) Shows  
 584 section 'A' from Fig. 1 - an axial view of the tibial plateau – including the ROI for MC, LC, ITB, and the  
 585 Second site. (b) Shows section 'B' – a more distal axial view of the plateau, including the head of fibula - the  
 586 ROI for LCL. (c) Shows section 'C' – a more distal axial view of the plateau at the level of the tibial tuberosity -  
 587 the ROI for PT. (d) Shows section 'D' – a midline sagittal view of the tibia - including the ROI for ACL and  
 588 PCL.  $\mu$ CT images taken from Tibia 5 (left tibia, female, age 76yrs, cause of death: heart failure). Image taken  
 589 during reconstruction on 08/03/19.

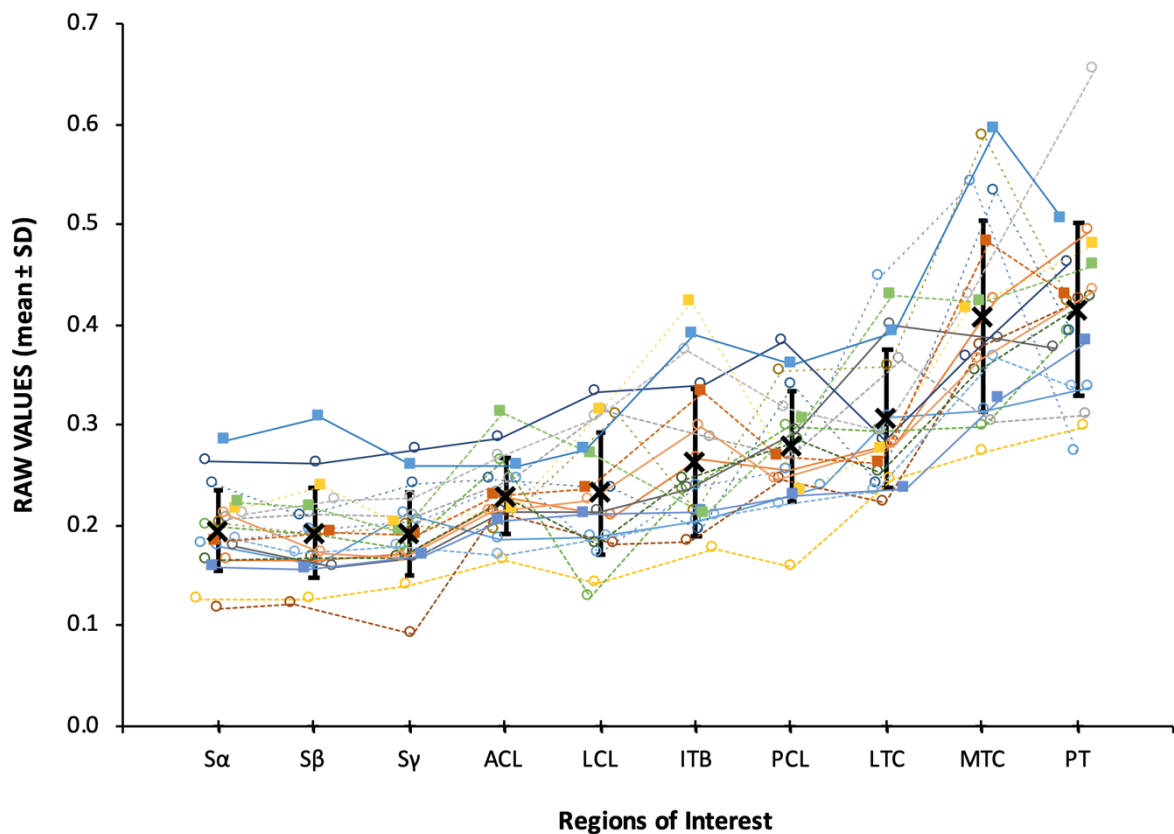


590  
 591  
 592  
 593  
 594  
 595  
 596  
 597  
 598  
 599  
 600  
 601  
 602  
 603

604 **Figure 3: Graph showing distribution of mean BV/TV and pooled mean BV/TV data across each regions**  
 605 **of interest.** (a) Mean BV/TV data from 20 subjects for 10 different loci on the tibia. Data from a single tibia are  
 606 connected by coloured lines. Filled squares: male tibiae. Open circles: female tibiae. Solid lines: right-sided.  
 607 Dashed lines: left-sided. Pooled mean BV/TV  $\pm$  SD shown in bold. (b) Logged mean BV/TV data from the  
 608 same complete dataset.

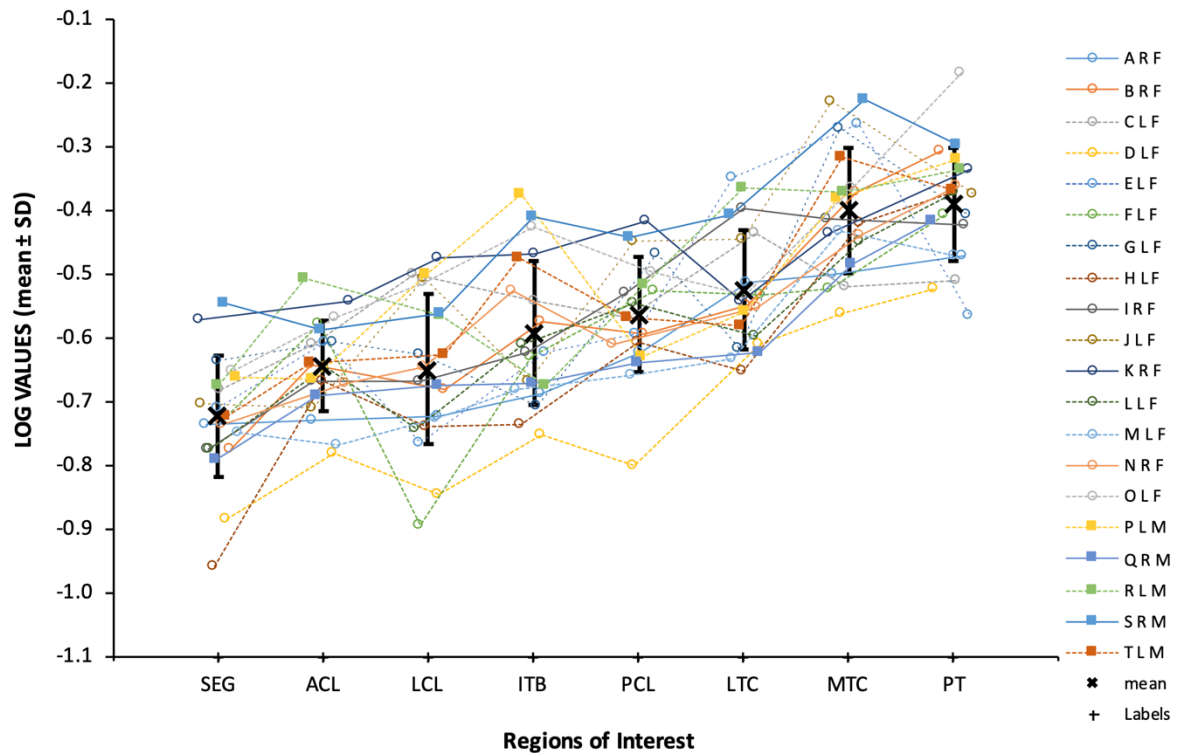


609

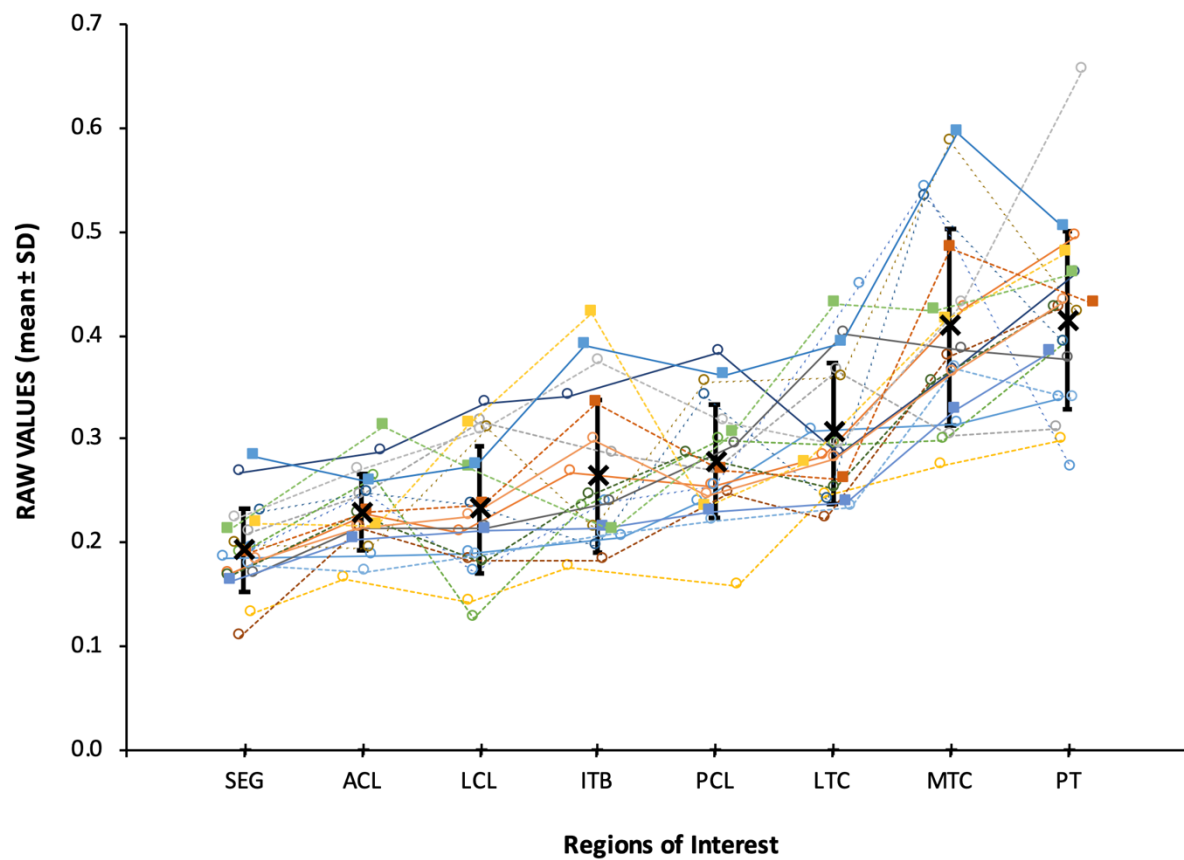


610  
611

612 **Figure S1: Graph showing distribution of mean BV/TV and pooled mean BV/TV data from the**  
 613 **condensed dataset.** (a) Mean BV/TV data from 20 subjects for 8 different loci on the tibia. SEG = mean of  $S\alpha$ ,  
 614  $S\beta$ ,  $S\gamma$ . Data from a single tibia are connected by coloured lines. Filled squares: male tibiae. Open circles:  
 615 female tibiae. Solid lines: right-sided. Dashed lines: left-sided. Pooled mean BV/TV  $\pm$  SD shown in bold. (b)  
 616 Logged mean BV/TV data from the same condensed dataset.



617



618